# On the nano-hillock formation induced by slow highly charged ions on insulator surfaces

C. Lemell [a,*], A.S. El-Said [b,1], W. Meissl [b], I.C. Gebeshuber [b], C. Trautmann [c], M. Toulemonde [d], J. Burgdörfer [a], F. Aumayr [b]

[a] *Institute for Theoretical Physics, Vienna University of Technology, 1040 Vienna, Austria*
[b] *Institut für Allgemeine Physik, Vienna University of Technology, 1040 Vienna, Austria*
[c] *Gesellschaft für Schwerionenforschung (GSI), 64291 Darmstadt, Germany*
[d] *Centre Interdisciplinaire de Recherches Ions Laser (CIRIL), Laboratoire commun CEA, CNRS, UCBN, ENSICAEN, BP5133, 14070 Caen Cedex 5, France*

The review of this paper was arranged by Prof. A. Zaslavsky

## Abstract

We discuss the creation of nano-sized protrusions on insulating surfaces using slow highly charged ions. This method holds the promise of forming regular structures on surfaces without inducing defects in deeper lying crystal layers. We find that only projectiles with a potential energy above a critical value are able to create hillocks. Below this threshold no surface modification is observed. This is similar to the track and hillock formation induced by swift (~GeV) heavy ions. We present a model for the conversion of potential energy stored in the projectiles into target-lattice excitations (heat) and discuss the possibility to create ordered structures using the guiding effect observed in insulating conical structures.
© 2007 Elsevier Ltd. All rights reserved.

## 1. Introduction

Controlled modification of surface and bulk properties of materials by irradiation with ion beams is a widely used technique in applied fields like microelectronics, biotechnology, or photonics [1]. Examples are ion implantation for local doping of devices and ion beam lithography for nanostructure fabrication. In these applications high ion fluences are used and the kinetic energy of the ions is adjusted in order to induce the desired surface modification [2]. With decreasing dimensions of devices, new experimental tools have to be developed. Recent work in this area has concentrated on employing individual slow highly charged ions (HCI) rather than intense singly charged ion beams.

Single ion implantation of slow highly charged ions [3] can be detected with nearly 100% efficiency using their high electron emission yields [4]. Together with a suitable lateral positioning system which allows the control of the ion impact site, arrays of single dopant atoms (as e.g. proposed for quantum computing [5]) could thus be produced. Due to the small range and straggling of slow HCI, placement accuracy would also be high in vertical direction (Fig. 1).

* Corresponding author.
*E-mail address:* lemell@concord.itp.tuwien.ac.at (C. Lemell).
[1] On leave from Physics Department, Faculty of Sciences, Mansoura University, 35516 Mansoura, Egypt.
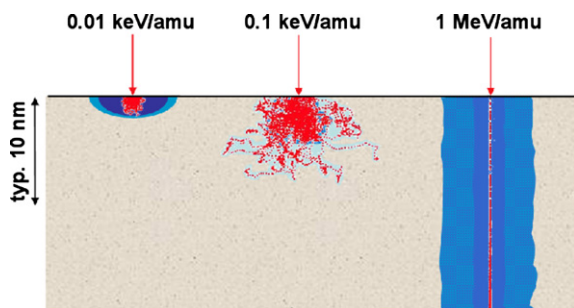
Fig. 1. Trajectories of heavy particles in matter: slow highly charged projectiles (left hand side) allow in principle for an exact positioning in both vertical and horizontal directions.

Surface modifications with only nanometer dimensions induced by single HCI impact have already been demonstrated [6–10] for various target-projectile combinations. During their recombination at a surface, slow HCI's deposit a large amount of potential energy into a small and shallow surface region [11,12], resulting in nano-sized surface defects (Fig. 1). Examples are the formation of $SiO_2$ nano-dots on a hydrogen passivated silicon surface [13] and the creation of nano-diamonds on HOPG [14] due to the impact of individual slow HCI. Carbon nanotubes can be grown selectively on such $SiO_2$ nanodots [15] or other catalytic spots. There is also hope that HCI irradiation spots show an increased and preferential chemical reactivity for particular biomolecules which would allow surface modifications for biological and biosensorical applications (e.g. selective protein absorption and immobilization, cell adhesion on bio-compatible surfaces, tissue engineering).

Current research therefore attempts to control the production of material modifications on surfaces and thin films with well-defined size in the nanometer region. One key control parameter is the potential energy of the HCI. This nano-structuring technique could further be combined with a precise positioning system for ion irradiation based on a tapered glass capillary system [16,17]. This is in contrast to swift heavy ions. For such projectiles it is difficult to form nano-beams required for exact positioning. Furthermore, swift ions penetrate deeply in the target leading to uncontrolled material mixing at semiconductor–insulator interfaces.

In this paper we briefly recall the experimental evidence for creation of nanostructures on $CaF_2$ surfaces [10] and present a first theoretical analysis of the observed potential energy threshold. Due to the small mismatch in lattice constants ($\sim$0.6%), $CaF_2$ can be epitaxially grown as insulator on silicon microelectronic devices [18–20]. Our findings may therefore be of importance for high resolution patterning of thin $CaF_2$ films on Si and for the creation of nanostructured templates for adlayer growth during fabrication of $CaF_2$/Si-based epitaxial insulator–semiconductor structures. Furthermore, we discuss a method to induce ordered surface defects using ion guiding through tapered glass capillaries [16,17].

## 2. Experimental evidence

Apart from its technological importance, $CaF_2$ features favorable material characteristics for investigations of hillock formation in HCI-surface interactions. $CaF_2(1\,1\,1)$ crystals can be air-cleaved resulting in atomically flat fluorine-terminated surfaces. After irradiation, samples have been reported to remain stable in atmosphere at room temperature [21] for several years.

Our samples were irradiated at the Heidelberg electron beam ion trap [22] using Ar and Xe ions with charge states ranging from 16 to 48. Typical fluences in the experiment range from 0.5 to $5 \times 10^9$ ions/cm$^2$. To investigate the effect of potential energy carried into the collision by the projectile, the kinetic energy of the impinging ions was in all cases below 10 kV extraction voltage times charge state $Q$ ($\leqslant$5 keV/amu). Hillock formation was monitored with atomic force microscopy (AFM) applying contact mode in air.

Fig. 2 shows examples of AFM topographic images of $CaF_2(1\,1\,1)$ after irradiation with $Xe^{28+}$ and $Xe^{46+}$ ions. Nano-sized protrusions with typical height of $h \approx 1$ nm and diameter $d \approx 50$ nm are observed on the surface for the higher charge state. An onset of hillock formation
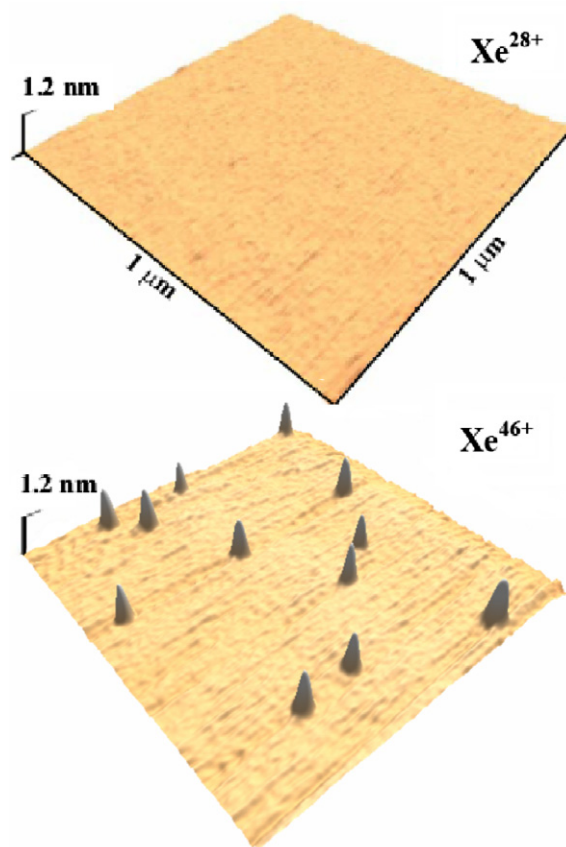


Fig. 2. AFM images of 1 μm × 1 μm of a $CaF_2$ surfaces irradiated with slow (keV/amu) $Xe^{28+}$ (top) and $Xe^{46+}$ ions (bottom). Note the vastly different lateral and vertical length scales.
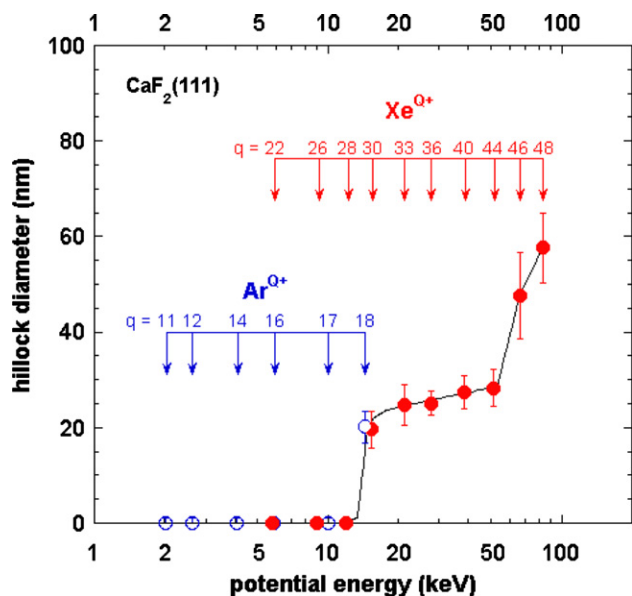
Fig. 3. Average diameter of nanohillocks on $CaF_2$ surfaces induced by highly charged ions. Apparent thresholds are observed around 14 and 50 keV (data from [10]).

was found between charge states $Q = 17$ and $Q = 18$ for Ar and $Q = 28$ and $Q = 30$ for Xe [10]. To probe for any kinetic energy dependence of the threshold, experiments were repeated with reduced projectile energies down to $1.5 \times Q$ keV ($< 0.6$ keV/amu at threshold, projected projectile range $\approx 25$ nm [23]). As the observed threshold charge states for Ar and Xe do not change, the kinetic energy can be ruled out as a dominant contribution to the process. Very recent preliminary data [24] at still lower energies ($0.15 \times Q$ keV) appear to support these findings. This is in contrast to the case of swift heavy ions, where a threshold was observed that depends on the energy loss ($S^{th} \geqslant 5$ keV/nm) and thereby on the kinetic energy of the projectile [21,25]. The diameter of the observed hillocks as a function of the potential energy carried into the collision by the HCI (Fig. 3) displays a sharp threshold at $E_{pot}^{th} \approx 14$ keV. For higher potential energies, the hillock diameter only slowly increases. At about $E_{pot} \approx 50$ keV, a second threshold appears characterized by a steep increase of $d$. The evolution of hillock height as a function of $E_{pot}$ follows a similar behavior.

## 3. Energy deposition and phase transition

In the following, we associate the two thresholds with phase transitions (melting and sublimation) induced by the HCI impact on the surface, i.e., to exciting the electronic subsystem by the potential energy carried into the collision by the HCI and the subsequent heating of the crystal by electron–phonon coupling [10]. Starting point of our interpretation is a modification of the so-called thermal-spike model developed for swift heavy ions [26]. The

model links track formation with local heating above the melting temperature and is based on a two-temperature model for the electronic and atomic subsystems with energy exchange by electron–phonon coupling.

As slow highly charged ions deposit only potential energy and penetrate the solid a few atomic layers, the energy deposition proceeds in a manner markedly different from that of swift heavy ions. In other words, the primary electron energy distributions $P_e(E)$ generated by a swift ion and a slow HCI, the starting point of the thermal spike, are fundamentally different. Unlike the kinetic energy of fast ions, only a fraction of the potential energy delivered by the ions is dynamically relevant to increase the energy density in the impact region. This is due to the fact that a significant fraction of the potential energy is stored in deep inner shell vacancies of the projectiles. The latter decay either radiatively or by emission of fast ($\sim$keV) electrons. In the former case, the energy is effectively lost for the heating while in the latter case the heating efficiency is much reduced. As slow ions cannot enter deeply into the target material, electrons have a large probability to escape into vacuum rather than to heat the crystal. For high energy electrons this probability reaches almost 50% and removes the corresponding energy available for lattice heating. Moreover, the main difference in potential energy between the sub-threshold charge state (e.g. $Ar^{17+}$) and the above-threshold charge state (e.g. $Ar^{18+}$) is exactly one additional vacancy. As this energy difference is released primarily by a fast electron, it appears obvious that the total potential energy cannot be the dynamically relevant quantity. For example, as the emission of one additional K-Auger electron close to the target surface is the main difference between the neutralization sequences of $Ar^{17+}$ and $Ar^{18+}$ ions, 50% of all $Ar^{18+}$ ions will deposit a similar amount of energy as $Ar^{17+}$, 25% of the $Ar^{18+}$ ions even much less (the energy of a single Ar K-Auger electron is about 3–4 keV). Still, the observed efficiency of $Ar^{18+}$ ions to create a hillock is close to 100% while for $Ar^{16+}$ and $Ar^{17+}$ projectiles it is effectively zero as no protrusions could be observed. Apparently, high-energy electrons effectively do not contribute to the formation of the thermal spike needed as starting point of the melting and sublimation processes.

### 3.1. Excitation of the electronic system

In order to gain deeper insight into the conversion of potential energy of a slow HCI into heating of the electronic degree of freedom which is the precursor of lattice heating, we simulate the neutralization sequence of the highly charged projectiles followed by a transport simulation for electrons emitted in the vicinity of $CaF_2$ surfaces. Neutralization of a highly charged projectile interacting with an insulating surface proceeds in two steps: as the ion approaches the surface, electron transfer to highly excited projectile states will set in [27–29]. These states are subsequently deexcited by Auger decay processes and radiative decay. Upon impact on the surface, projectile

states are quickly shifted upwards in energy due to the self-image interaction. As a consequence, excited states are reionized. When entering the target material, a large fraction of the projectiles are still highly charged. The deexcitation sequence now only involves states below or in resonance with the insulators valence band.

We simulate this process using the classical-over-the-barrier model [27] which has been successfully extended to simulate electron transfer processes at and below metal and insulator surfaces [30]. Mainly, classically allowed electron transfer into excited states initiates a deexcitation sequence via Auger and radiative decay processes. The screening of the projectile core due to the increasing target electron density and therefore the shift of energy levels with respect to their vacuum position is taken into account properly. As alternative to resonant electron capture we also allow for Auger capture processes, i.e., both interacting electrons originate in the target valence band with one of them populating an inner shell of the projectile and the other carrying the excess kinetic energy. All electrons emitted during the neutralization of the HCI enter as input to the subsequent electron-transport simulation.

### 3.2. Electron transport and lattice heating

The transfer of electrons to the projectile leaves unbalanced holes in the surface which store part of the potential energy of the HCI. They diffuse only slowly into the material (hole velocity in the valence band derived from tight-binding calculations is smaller than 0.33 nm/fs [31]). Furthermore, two holes ($F^0$ atoms) in adjacent sites recombine to volatile fluorine gas molecules leaving behind a Ca-enriched metallic region. Details of the metallic island formation and their effect on electron transport are, however, not known. We therefore restrict ourselves to modeling of electron transport through $CaF_2$ without taking the influence of the lattice structure on the electron trajectories into account [32,33]. In the simulation, the transport of an electron through the medium is approximated as a classical zig-zag trajectory. Deflections are caused by stochastic elastic and inelastic scattering processes. Between two subsequent scattering events, an electron covers a distance of $\lambda_{tot}$ with $\lambda_{tot}^{-1} = \lambda_e^{-1} + \lambda_{in}^{-1}$ where $\lambda_e$ and $\lambda_{in}$ are the elastic and inelastic mean free paths shown in Fig. 4, respectively. Scattering probabilities are calculated based on optical data for the dielectric function of $CaF_2$ [34] and an extrapolation to non-zero momentum transfer [35]. We assume that inelastic processes lead to an energy loss $\Delta E$ of the primary electron and the creation of a secondary electron with an initial kinetic energy of $\Delta E$. Also, these cascade electrons are followed along their subsequent trajectories. Elastic scattering, more precisely, elastic scattering in the electronic degree of freedom, in turn, couples the electronic system to the target lattice. We assign every elastic scattering event a probability to excite a phonon ($E_{ph} \approx 0.06$ eV). If a phonon is excited, the position of creation is recorded adding to the heating of the target crystal.
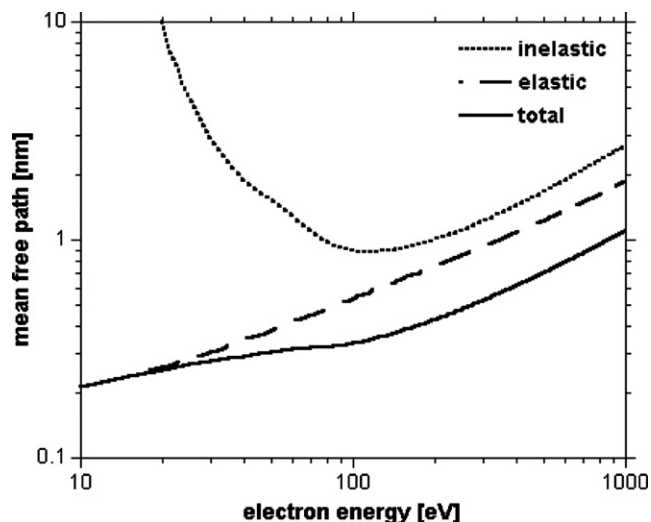


Fig. 4. Inelastic, elastic, and total mean free paths in $CaF_2$ calculated from optical data [34].

### 3.3. Model results

The dominance of elastic over inelastic scattering signified by the much smaller mean free path (Fig. 4) over a wide range of low to intermediate electronic energies clearly points to a bias towards lower energies in the heating efficiency of the primary electrons. While low energy electrons undergo a large number of (primarily elastic) collisions thereby exciting a large number of phonons within a small volume around their point of emission, high energy electrons travel more than one order of magnitude farther (see $\lambda_{tot}$ in Fig. 4) before interacting with the target material. Although in total much more energy is deposited, the resulting energy *density* is very small. The average energy density distributed following the emission of one primary electron (containing contributions from secondary
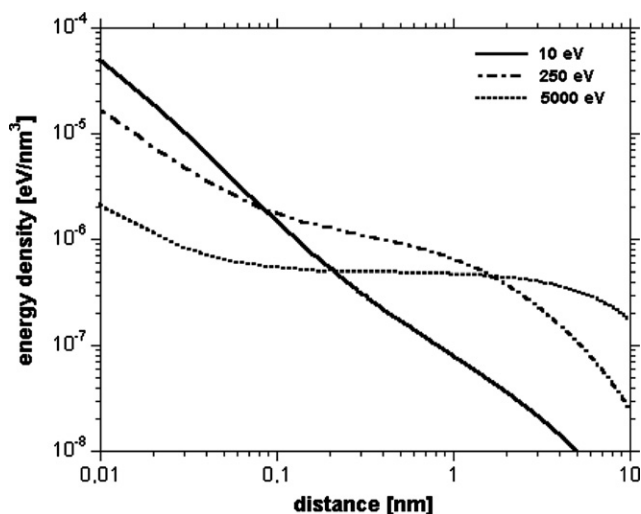


Fig. 5. Average energy deposition of electrons with 10, 250, and 5000 eV kinetic energy above the vacuum level as a function of distance from the point of emission.

electrons) as a function of distance from the point of emission (Fig. 5) illustrates the difference in heating efficiency: at small distances, low energy electrons heat up the lattice much more efficiently (note the double logarithmic scale) than high energy electrons. The formation of a thermal spike is therefore primarily driven by electrons with energies up to a few hundred eV only.

It is now instructive to analyze the emission spectrum $P_e(E)$ of different HCI. Examples for $Ar^{18+}$ and $Xe^{30+}$ calculated within the classical-over-the-barrier model (see Section 3.1), both just above the threshold for hillock formation, are shown in Fig. 6. Although electron emission spectra of Ar and Xe ions are different in detail (see Fig. 6), the total number of electrons with energies $\leqslant 350$ eV is almost identical.

We introduce an initially somewhat arbitrary energy cut-off at $E_{cut} = 350$ eV emission energy. At this energy, the elastic mean free path reaches 1 nm which is the characteristic length scale for both the height of the hillock as well as the penetration depth of the HCI. For this choice of $E_{cut}$ we plot the relation between the charge state and the effectively deposited energy (Fig. 7). Experimentally, the threshold is found between charge states with $-1 \leqslant Q - Q_{th} \leqslant 0$. In our simulation, this corresponds to an effective energy deposition of about 2 keV (gray shaded area). Data for $Xe^{29+}$ (open circle with $Q - Q_{th} = -1$ within the transition region) have not yet been measured. Remarkably, the deposited energies at threshold charges agrees for Ar and Xe ions (i.e., they coincide near $Q - Q_{th} \approx 0$) while they differ for other charges. The point to be emphasized is that the difference between the sub-threshold $Ar^{17+}$ and the above-threshold $Ar^{18+}$ ion is not the additional K-Auger electron but the additional slow electrons ($\leqslant 350$ eV) emitted along the relaxation cascade in the neutralization sequence of the HCI. Neglecting radiative decay processes, only Auger transitions are responsi-
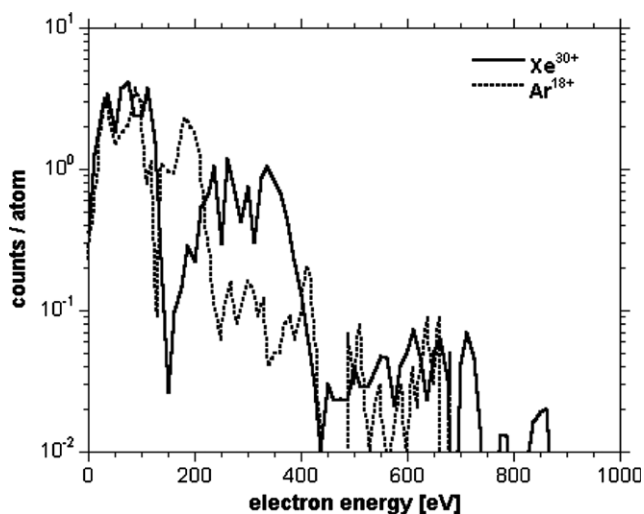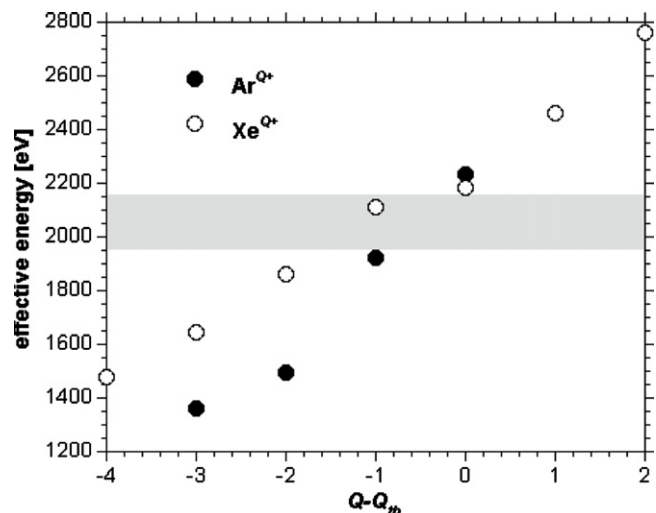


Fig. 7. Relation between effective energy deposition (total energy of electrons emitted with less than 350 eV) and threshold charge stet $Q - Q_{th}$ for different ionic species of Ar ($Q_{th}^{Ar} = 18$) and Xe ($Q_{th}^{Xe} = 30$). The threshold lies between $-1 \leqslant Q - Q_{th} \leqslant 0$. The critical energy deposition needed is indicated by the shaded area.

ble for inner-shell filling of the HCI. The additional K-shell hole in $Ar^{18+}$ will not only induce the emission of one more K-Auger and two more L-Auger electrons with energies higher than $E_{cut}$ but also the emission of four more M-Auger electrons with energies between 200 and 400 eV (see Fig. 6). In the full simulation, we find that $Ar^{17+}$ emits on average 15 electrons with kinetic energies smaller than 350 eV into the material, $Ar^{18+}$ on average 18.1 electrons which is close to the estimate. A similar difference is found for $Xe^{28+}$ and $Xe^{30+}$ ions which deposit 16 and 18.7 electrons below $E_{cut}$, respectively. It is important to note that the results presented here are not sensitive to the specific choice of $E_{cut}$ as long as low to intermediate energy electrons with mean free paths up to the order of 1 nm are included.

The deposited energy is contained in a small volume. To gain a rough estimate, we assume the energy to be uniformly distributed within a half sphere of 1 nm radius in accordance with our choice for $E_{cut}$. Under these conditions, an energy density of $\sim 2000$ eV/$V \approx 950$ eV/nm$^3$ or $\sim 13$ eV/atom is reached. The energy will quickly be spread over a larger volume by heat transport through the material. The energy density drops for a radius $> 3$ nm to below the density required for melting (0.55 eV/atom). Despite the fundamental difference in the underlying electronic processes, this energy density is remarkably close to the density reached by the thermal spike produced by swift GeV ions.

We have thus established a surprisingly close correspondence to the thermal spike model for swift heavy ions in terms of the initial energy deposition in the electronic degree of freedom. As for high-energy ions, the ensuing melting dynamics itself is not yet well understood. Studies on the etchability of swift ion tracks in LiF [36] suggest an irreversible clustering of lattice defects (color centers) as



Fig. 6. Electron emission spectrum of $Ar^{18+}$ and $Xe^{30+}$ within a CaF$_2$ crystal. Electrons with less than 350 eV initial kinetic energy contribute equally to the lattice heating for both projectiles.

necessary precursor for restructurization of the target material. This clustering is only observed in the inner part of the ion track. It is accompanied by the extraction of a large number of target electrons along the track of the projectile and, possibly, by expansion of the central area due to Coulomb repulsion. This process is sustained by the small mobility of valence band electrons. This may also explain the discrepancy between the area of high energy density ($r \approx 3$ nm) and the large hillock diameter of some 20 nm: A swelling inner part along the ion track could reshape a large target volume due to the high density of defects and therefore reduced stability of the lattice.

## 4. Ordered surface structuring

One intriguing challenge is the production of ordered patterns of nanohillocks by HCI impact on insulator surfaces. Our discussion was, so far, limited to random impact points of the projectiles (see Fig. 2). Recently, a new pathway for controlled projectile positioning has opened: based on self-organized guiding of charged particles through nanocapillaries without change of the initial charge state. This effect has been observed for the first time by Stolterfoht et al. [37]. Meanwhile, the guiding effect of insulating nanocapillaries has been reported for various insulating materials. The following theoretical scenario has been developed to understand the guiding effect [38]: in the early stage of the irradiation, projectiles hit the inner wall of the capillary and deposit their charge on the insulating surface. These charges diffuse along the surface and, eventually, into the bulk due to the small but finite surface and bulk conductivities of the insulator. Projectiles entering the capillary at a later stage are deflected by the Coulomb field of the self-organized charge patch close to the entrance of the capillary along the capillary axis. This effect has lately been exploited for guiding through a funnel-shaped capillary target of fast singly charged ions [39] and for slow HCI [16,17]. Ion beams are compressed by the guiding effect and exit the funnel structure with a beam divergence smaller than the nominal opening angle (difference in entrance and exit diameters over length of funnel). Current density enhancements by a factor of $10^2$–$10^4$ have been reached

by reducing the exit diameter of the funnel to about 100 nm. By further reducing the exit diameter, preselected impact points can be addressed allowing for fabrication of ordered hillock patterns (Fig. 8).

In conclusion, we have introduced a model to account for hillock formation by highly charged ion impact on insulating material surfaces. It is found that only a fraction of the total potential energy carried into the collision by the HCI effectively contributes to the heating of the crystal lattice. We have also discussed a pathway to inducing ordered structures on surfaces using self-organized guiding through funnel-shaped nanocapillaries.

## Acknowledgements

## References

[1] Köhler M. Nanotechnology. Weinheim: Wiley-VCH; 2001.
[2] Hanley L, Sinnott SB. Surf Sci 2002;500:500.
[3] Schenkel T et al. Nucl Instrum Meth Phys Res B 2004;219-220:200.
[4] Aumayr F, Kurz H, Schneider D, Briere MA, McDonald JW, Cunningham CE, et al. Phys Rev Lett 1993;71:1943.
[5] Kane BE. Nature 1998;393:133.
[6] Schneider DH, Briere MA, McDonald J, Biersack J. Rad Eff Def Solid 1993;127:113.
[7] Parks DC, Stöckli MP, Bell EW, Ratliff LP, Schmieder LW, Serpa FG, et al. Nucl Instrum Meth Phys Res B 1998;134:46.
[8] Ratliff LP, Bell EW, Parks DC, Pikin AI, Gillaspy JD. Appl Phys Lett 1999;75:590.
[9] Hayderer G, Cernusca S, Schmid M, Varga P, Winter HP, Aumayr F. Phys Scripta 2000;T92:156.
[10] El-Said AS, Meissl W, Simon MC, Crespo López-Urrutia JR, Lemell C, Burgdörfer J, et al. Nucl Instrum Meth Phys Res B 2007;258:167.
[11] Arnau A et al. Surf Sci Rep 1997;27:113.
[12] Aumayr F, Winter HP. Phil Trans Roy Soc London 2004;362:77.
[13] Borsoni G et al. Solid-State Electron 2002;46:1855.
[14] Meguro T, Hida H, Suzuki M, Koguchi K, Takai H, Yamamoto Y, et al. Appl Phys Lett 2001;79:3866.
[15] Wei BQ, Vajtai R, Jung Y, Ward J, Zhang R, Ramanath G, et al. Nature 2002;416:495.
[16] Ikeda T et al. Appl Phys Lett 2006;89:163502.
[17] Cassimi A, et al. Int J Nanotechnol, submitted for publication.
[18] Smith TP, Phillips JM, Augustyniak WM, Stils PJ. Appl Phys Lett 1984;45:907.
[19] Schowalter LJ, Fathauer RW. J Vac Sci Technol 1986;4:1026.
[20] Lucas CA, Loretto D. Appl Phys Lett 1992;60:2071.
[21] Khalfaoui N, Rotaru CC, Bouffard S, Toulemonde M, Stoquert JP, Haas F, et al. Nucl Instrum Meth Phys Res B 2005;240:819.
[22] Crespo López-Urrutia JR et al. Hyperfine Interact 2003;146/147:109.
[23] Ziegler JF, Biersack JP, Littmark U. The stopping and range of ions in solids. New York: Pergamon Press; 1984, SRIM2006, http://www.srim.org.
[24] El-Said AS, et al. Phys Rev B, in preparation.
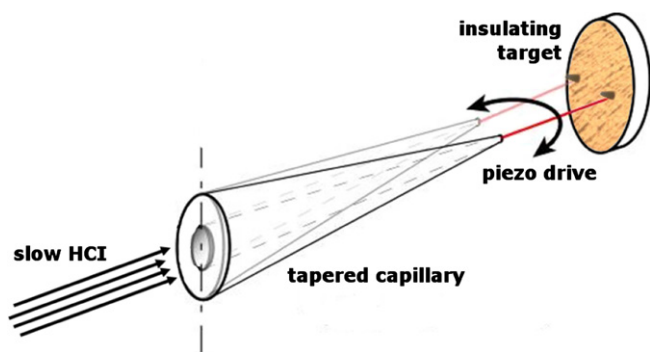[25] El-Said AS, Cranney M, Ishikawa N, Iwase A, Neumann R, Schwartz K, et al. Nucl Instrum Meth B 2004;218:492;

Fig. 8. Schematic experimental setup for hillock formation by guided nanobeams of HCI [16].

Müller C, Benyagoub A, Lang M, Neumann R, Schwartz K, Toulemonde M, et al. Nucl Instrum Meth B 2003;209:175.

[26] Toulemonde M, Dufour Ch, Meftah A, Paumier E. Nucl Instrum Meth B 2000;166/167:903.

[27] Burgdörfer J, Lerner P, Meyer FW. Phys Rev A 1991;44:5674.

[28] Hägg L, Reinhold CO, Burgdörfer J. Phys Rev A 1997;55:2097.

[29] Wirtz L, Reinhold CO, Lemell C, Burgdörfer J. Phys Rev A 2003;67:12903.

[30] Burgdörfer J, Reinhold CO, Meyer FW. Nucl Instrum Meth Phys Res B 1995;98:415.

[31] Albert JP, Jouanin C, Gout C. Phys Rev B 1977;16:925.

[32] Tökesi K, Varga D, Köver L, Mukoyama T. J Electron Spectrosc Rel Phenom 1995;76:427.

[33] Solleder B, Lemell C, Tökesi K, Hatcher N, Burgdörfer J. Phys Rev B, accepted for publication.

[34] Palik ED, editor. Handbook of optical constants of solids II. Academic Press Inc; 1991.

[35] Reinhold CO, Burgdörfer J. Phys Rev A 1997;55:450.

[36] Trautmann C, Schwartz K, Geiss O. J Appl Phys 1998;83:3560.

[37] Stolterfoht N, Bremer JH, Hoffmann V, Hellhammer R, Fink D, Petrov A, et al. Phys Rev Lett 2002;88:133201.

[38] Schiessl K, Palfinger W, Tökesi K, Lemell C, Nowotny H, Burgdörfer J. Phys Rev A 2005;72:062902.

[39] Nebiki T et al. J Vac Sci Technol 2003;A21:1671.